ELSEVIER

Contents lists available at ScienceDirect

# Advances in Water Resources

journal homepage: www.elsevier.com/locate/advwatres





# Grid edge classification method to enhance levee resolution in dual-grid flood inundation models

Daniel T. Kahl<sup>a</sup>, Jochen E. Schubert<sup>a</sup>, Ariane Jong-Levinger<sup>a</sup>, Brett F. Sanders<sup>a,b,\*</sup>

- a Department of Civil and Environmental Engineering, UC Irvine, Irvine, CA 92697, USA
- <sup>b</sup> Department of Urban Planning and Public Policy, UC Irvine, Irvine, CA 92697, USA

# ARTICLE INFO

Keywords: Flood risk Inundation Levees Urban flooding Hazards

# ABSTRACT

Dual-grid models address the computational bottlenecks of large-scale (> 10<sup>3</sup> km²) urban flood modeling with solution updates on a coarse grid that are informed by topographic data on a fine grid. However, dual-grid models may poorly resolve levees, leading to loss of accuracy. Here we present a grid edge classification method whereby specific edges of the coarse grid are flagged to gather nearby topographic data from the fine grid and create a contiguous physical barrier. The method relies on levee location data in a polyline format, and does not require levee height data since that information is stored on the fine grid. Using a 6804 km² model of the Los Angeles Metropolitan Region with 3 m topographic data and 987 km of levees, the proposed method is implemented and evaluated. Simulations using coarse grids of 15, 30 and 60 m capture flood extent consistent with fine-grid models based on a critical success index (CSI) of 90, 87 and 82%, respectively. Edge classification improves CSI up to 7 percentage points over a model with unclassified coarse grid edges, and reduces the false alarm ratio up to 10 percentage points. Differences in model performance across the study area are noted, including lower accuracy on urbanized alluvial fans. With compute costs that scale with the coarse grid, dual-grid models can efficiently realize more accurate large-scale models of urban flood hazards.

## 1. Introduction

Flooding from extreme weather events including tropical storms, storm surge, heavy rainfall and flash floods poses major risks to human populations, assets and economic activities. Flood losses have been on the rise for decades both in the U.S. and globally, while fatalities have fallen over the same period (Gall et al., 2011; WMO, 2021). The five largest disasters ever recorded, when measured by economic losses, were hurricanes Katrina, Sandy, Irma, Harvey, and Maria, and involved significant flooding in addition to wind and other storm damage (WMO, 2021). Moreover, flood impacts are increasingly concentrated in urban areas characterized by high population densities and high physical and social vulnerabilities (Galloway et al., 2018; Hino and Nance, 2021), and there have been calls for new approaches and strategies to curb impacts and build resilience (Task Committee on Flood Safety Policies and Practices, 2014; NASEM, 2019).

Spatially distributed flood hazard (inundation) modeling is important for characterizing risks and assisting flood risk adaptation processes (Ward et al., 2015; Sanders et al., 2020; Bates et al., 2021; Wing et al., 2022). Flood simulations have supported adaptation at local levels for decades by enabling the mapping of flood zones, the

guidance of mitigation measures such as levees and drainage infrastructure, and planning for physical vulnerability reduction through land-use and zoning restrictions (NRC, 2009). Recently, large-scale (defined here as  $> 10^3$  km<sup>2</sup>) flood simulation models have been developed to support national-level and international risk management needs, including data for insurance schemes, identification of global flood risk hot spots, and planning of sustainable development (Ward et al., 2015).

Large-scale (national, continental and/or global) flood hazard modeling has mainly been pursued with modeling frameworks of two different types: statistical/hydrologic and hydrologic/statistical. The statistical/hydrologic approach begins with available statistics on flood hazard drivers, such as rainfall and streamflow, and continues with the application of a hydrodynamic flood inundation model on a regional domain to map flood hazards (Sampson et al., 2015; Dottori et al., 2016; Schumann et al., 2016). National, continental, and/or global coverage is subsequently achieved by assembling results of numerous regional models. Conversely, the hydrologic/statistical approach begins with simulating the hydrologic cycle over the scale of interest (national, continental, global) to generate a spatially distributed data set of peak flood volumes (e.g., annual maxima). Next, a probability distribution is

https://doi.org/10.1016/j.advwatres.2022.104287

<sup>\*</sup> Corresponding author at: Department of Civil and Environmental Engineering, UC Irvine, Irvine, CA 92697, USA. *E-mail address:* bsanders@uci.edu (B.F. Sanders).

URL: http://www.floodlab.eng.uci.edu (B.F. Sanders).

fit to model output to estimate extremes, and in a third step, extreme flood volumes are downscaled with the aid of topographic data to map hazard distributions over the large-scale domain (Pappenberger et al., 2012; Winsemius et al., 2013). Both the statistical/hydrologic method and the hydrologic/statistical method have proven successful at advancing understanding of present and future risks at large scales. For example, household-level flood risk and inequities have been estimated for the continental U.S. based on a statistical/hydrologic framework (Bates et al., 2021; Wing et al., 2022), and the hydrologic/statistical framework has enabled global estimation of future flood risk (Winsemius et al., 2016), critical insights into strategies to manage future riverine flooding (Jongman et al., 2015) and guidance for provision of aid and assistance during flooding disasters (Ward et al., 2015).

One of the weaknesses of large-scale modeling frameworks is that flood hazards in urban areas, where population density and physical and social vulnerabilities are greatest, are somewhat crudely estimated (Jonkman, 2013). For example, Ward et al. (2017) report a median critical success index of only 46% across eight urban areas within the U.S., U.K., Germany and Thailand for estimation of the 100year flood zone, and Wing et al. (2017) report a critical success index of 23% for areas of the U.S. classified as "High Intensity Development" based on data from the National Land Cover Database. Large-scale flood models tend to use somewhat coarse grids by urban flood modeling standards, and also lack sensitivity to flood management infrastructure, which is essential for shaping flood risk adaptation (Jonkman, 2013). Urban flood modeling is now a relatively mature field following decades of research into model structure and numerical methods (Teng et al., 2017; Guo et al., 2021; Dewals et al., 2021; Mignot and Dewals, 2022), and thus methods for accurate urban flood modeling are well known including reliance on local knowledge, urban drainage infrastructure data, and sufficient grid resolution to resolve flow paths and obstructions (Jonkman, 2013). The main barriers facing large-scale modeling are that: (1) detailed data relied upon by urban flood models are not widely available to support large-scale modeling (Ward et al., 2015), and (2) the computational and memory demands of fine-grid urban flood modeling (e.g., Russo et al., 2015) become prohibitively expensive at large scales (Sanders et al., 2010; Ivanov et al., 2021). Considerable recent research has been directed at overcoming the computational bottlenecks of urban flood modeling. For example, Mignot and Dewals (2022) review a number of different methods including using graphical processing units (GPUs), porosity models, and fast surrogate models (Dewals et al., 2021; Ivanov et al., 2021; Mignot and Dewals, 2022). Of these, applications at large scale have mostly used fast surrogate model approaches (Dewals et al., 2021).

Dual-grid modeling approaches have recently emerged as a highly promising approach to overcome the computational challenges of largescale urban flood modeling described above. Derived from multigrid approaches to solving the hydrodynamic equations governing flood inundation (Stelling, 2012; Henonin et al., 2013), dual-grid models are limited to two grid resolutions: a fine-resolution grid to resolve topographic data and a coarse-resolution grid for solution updates (Volp et al., 2013; Sanders and Schubert, 2019; Shamkhalchian and De Almeida, 2021). Cartesian grids are used to simplify data structures for upscaling and downscaling and to simplify data management, which is paramount in large-scale flooding applications due to high data volumes. Dual-grid models can also support ideal parallel scaling, enabling simulation domains of any size given available computational resources due to well-balanced data structures (Sanders and Schubert, 2019). Here, we refer to the fine grid of topographic data with a resolution  $\Delta_z$  as the Zgrid and the coarse grid with a resolution  $\Delta_U$  as the Ugrid. The Zgrid is also known as a Digital Elevation Model (DEM), while the Ugrid is the basis for mass conservation and momentum balance updates. The ratio of grid sizes represents the upscale factor,  $\alpha = \Delta_U/\Delta_z$ , and practical applications of the dualgrid Parallel Raster Inundation Model (PRIMo) with  $\alpha$  ranging from

10–20 have been shown to reduce computational costs by orders of magnitude compared to fine-grid modeling, without overly sacrificing accuracy (Sanders and Schubert, 2019).

Dual-grid models are a type of subgrid model, which refers to any type of analytical or empirical model that calculates the solution at scales finer than the Ugrid resolution. Examples of subgrid models include multi-grid models (Hénonin et al., 2015; Stelling, 2012), porosity models (Dewals et al., 2021), analytical models of subgrid-scale channel flows (Neal et al., 2012) and data-driven empirical models of storage, conveyance and flow resistance (Casulli and Stelling, 2011; Brunner, 2022). The general idea behind subgrid models is to leverage knowledge about fine-resolution details that affect flood inundation, such as the shape of the land surface resolved on a Zgrid (e.g., Casulli and Stelling, 2011), the width of a channel visible from aerial imagery (e.g., Neal et al., 2012), or the presence of blockage features that affect floodplain storage and conveyance (e.g., Sanders et al., 2008), while avoiding prohibitively high compute costs.

The development of subgrid models in general, and dual-grid models in particular, has also led to new approaches to the representation of flood management infrastructure such as curb inlets, subsurface pipes and pumps at the scale of the Ugrid. For example, to account for drainage from curb inlets through pipes to flood channels, PRIMo can use pairs of inlets and outlets that transfer water between Ugrid cells, which can be done sequentially in the solution update process without negatively impacting parallel scaling that is crucial for model efficiency at large scales (Sanders and Schubert, 2019). For each hydraulic link, flow is routed from the inlet to the outlet each time step in accordance with the type and size of the infrastructure (Chang et al., 2018). When applied to the historical Baldwin Hills dam-break flood scenario (Gallegos et al., 2009), an uncalibrated dual-grid PRIMo model simulated inundation with a critical success index of 70% using an upscale factor of 10 and previously reported drainage infrastructure parameters (Sanders and Schubert, 2019).

Delineating blockage and overtopping features such as levees and flood walls is of paramount importance when developing flood hazard models for both urban and rural areas, and especially when using a subgrid model because the widths of Ugrid cells are likely to be coarse compared to levee widths. Sanders and Schubert (2019) demonstrated that with increased upscaling of a dual-grid model, representation of blockage features progressively worsened. Unstructured grid models address this problem by positioning edges of the computational mesh along levee crests to directly resolve the blockage feature (Brunner, 2022; Gallien et al., 2011; Luke et al., 2015), while structured grid models resolve blockage features by moving the location (and in some cases, the width) of the levee to the nearest topographic cell (Wing et al., 2019a; Shustikova et al., 2020). Moreover, frameworks that automate the representation of blockage features in flood inundation models have been a focal point of research. Hodges (2015) and Li and Hodges (2019, 2020) presented a semi-automated approach that begins by calculating an elevation differential raster between the Zgrid the Ugrid. Values above a specified cutoff height in the differential raster signify unresolved features on the Ugrid, and the connected nonzero values are registered as blockage features that are transferred to the nearest coarse grid edges. Wing et al. (2019b) developed a method whereby five geomorphometric characteristics of the Zgrid were computed as indicators of levee features, a probabilistic model for levee features was trained using known levee locations from the U.S. Army Corps of Engineers (USACE) National Levee Database (USACE, 2015), and then selected grid cells of the hazard model were elevated to represent the blockage feature. In summary, previous work shows that accurately representing blockage features is an important and especially challenging aspect of flood inundation modeling using subgrid models. Furthermore, in the context of dual-grid models, previous research points to value of methods that register the location of blockage features on the Ugrid, and adapt the processing of Zgrid data for solution updates depending on the presence or absence of blockage features.

Data to improve the representation of levees in flood inundation models is increasingly available. The National Levee Database (USACE, 2015) contains data on over 7,000 levee systems spanning over 40,000 km in the U.S., and the database is constantly being updated due to efforts from local, state, federal and tribal agencies. There have also been calls for regional to global infrastructure data (Tourment et al., 2018; Özer et al., 2020), and a new international levee database, open-DELVE, was recently introduced (O'Dell et al., 2021). High-resolution Zgrid data is also widely available across urban areas of developed nations to support detailed inundation modeling, and the need for greater global coverage of high-quality topographic data has been recognized (Schumann and Bates, 2020).

The purpose of this study is to present a new, semi-automated method to improve the representation of blockage features in dualgrid flood inundation models based on the following preconditions consistent with the literature review above: (a) the location and continuity of flow barriers have been characterized as a polyline, or can be readily characterized as a polyline using geospatial tools and data, and (b) data characterizing the height of obstructions such as levees are resolved on the Zgrid. Specifically, in this study we present a semiautomated workflow that flags Ugrid edges based on the presence of a barrier (levee) so that the flow solver is guided to enforce blockage effects when such features are present and simulate overtopping when flood levels exceed blockage feature heights. Hence, herein we present a workflow for Ugrid edge classification that enables the dual-grid solver to utilize available topographic data for solution updates more intelligently, with the aim of achieving fine-grid model accuracy at the computational cost of running a coarse-grid model. We acknowledge possible exceptions to the preconditions above, such as errors in levee polyline data and blockage features that are not resolved by the Zgrid, but argue that these exceptions can be addressed with additional editing and processing of data, and thus a push towards a semi-automated workflow could offer immense value for future modeling.

The remainder of the paper continues as follows: Methods, including the proposed grid edge classification method, are presented in Section 2, Applications of the method and results are presented in Section 3, and we close with Discussion (Section 4) and Summary and Conclusion (Section 5).

## 2. Methods

## 2.1. Large-scale flood hazard model

PRIMo simulates flood hazards by solving the two-dimensional shallow-water equations with a Godunov-type finite volume scheme that is conditionally stable in accordance with a Courant-Friedrichs-Lewy (CFL) condition (Sanders and Schubert, 2019). Simulations can be forced in several different ways: spatially distributed and time-varying precipitation (non-point sources), time-varying inputs from streams entering a model domain and/or concentrated runoff from catchments (point sources), time-varying water levels at model domain boundaries (boundary water levels), and point sink/point source pairs that account for water transfers through storm water infrastructure such as drainage pipes (water transfers). Additionally, flow resistance is modeled using a spatially distributed Manning resistance parameter, and soil infiltration is modeled with a runoff coefficient that transforms precipitation into runoff (Noh et al., 2019) and approaches unity in urban areas due to impervious surfaces and soil saturation during extreme events (Bates et al., 2010; Wing et al., 2017; Noh et al., 2019). For this study, emphasis is placed on fluvial flooding scenarios to document potential overtopping of levees, and thus model forcing is based on point sources of streamflow added to drainage channels that are representative of lateral inflows.

The fine-resolution Zgrid used by PRIMo corresponds to a DEM with  $n_x$  columns and  $n_y$  rows of ground elevation data,  $z_{i,i}$  for i = $1, \ldots, n_x$  and  $j = 1, \ldots, n_y$ , with a uniform cell size of  $\Delta_z$ . Here, i and i represent indices in a conventional Cartesian coordinate system with the origin in the lower-left corner of the spatial domain. The coarseresolution Ugrid corresponds to a spatial domain congruent with the Zgrid where the number of columns and rows is based on the upscale factor,  $N_x = n_x/\alpha$  and  $N_y = n_y/\alpha$ , respectively. Introducing capitalized indices for the coarse grid,  $I = 1, ..., N_x$  and  $J = 1, ..., N_y$ , the solution state in each coarse-grid cell is given by  $U_{IJ} = (\eta_{IJ} \quad p_{IJ} \quad q_{IJ})$ where  $\eta$  represents the elevation of the water surface, p represents the discharge per unit width in the x direction, and q represents the discharge per unit width in the y direction. Furthermore, slopes in the free surface elevation,  $(\delta_x \eta)_{I,J}$  and  $(\delta_v \eta)_{I,J}$  are computed using the minmod limiter (Sanders and Bradford, 2006) and used to downscale flood depth, d, from the Ugrid to the Zgrid as follows:  $d_{i,j}$  =  $\max(\eta_{i,j}^* - z_{i,j}, 0)$  for  $i = \alpha(I - 1) + 1, ..., \alpha I$  and  $j = \alpha(J - 1) + 1, ..., \alpha J$ 

$$\eta_{i,j}^* = \eta_{I,J} + (\delta_x \eta)_{I,J} \times (x_i - \overline{x}_I) + (\delta_y \eta)_{I,J} \times (y_j - \overline{y}_J) \tag{1}$$

and where  $\overline{x}_I$  and  $\overline{y}_J$  represent cell-centered coordinates on the Ugrid. PRIMo leverages the dual-grid data structure in three distinct ways to support accurate flood hazard modeling. First, the  $\alpha^2$  z values within each Ugrid cell are used to create tables of water storage per unit area, h, versus water level  $\eta$ . Once established in a pre-processing step, these tables are used each time step to compute  $\eta$  in each cell based on the storage, h, computed from the mass balance equation. Second, the  $2\alpha$  z values from the two sides of each Ugrid edge are used to establish the cross-sectional shape for mass and momentum fluxes between neighboring cells,  $\hat{z}_k$ ,  $k = 1 \dots \alpha$ , including momentum fluxes that account for the bed slope source term (Valiani and Begnudelli, 2006). And third, PRIMo uses a bilinear reconstruction of the free surface elevation (Eq. (1)) for accurate downscaling of flood depth (Bradford and Sanders, 2005). Note that the weakness of PRIMo addressed herein, the representation of blockage effects, relates to the estimation of  $\hat{z}_k$ ,  $k = 1 \dots \alpha$ , for each Ugrid edge connecting neighboring cells.

# 2.2. Study area and supporting data

The proposed Ugrid edge classification method is presented in the context of the Los Angeles Metropolitan Region (Fig. 1), home to the 8<sup>th</sup> largest megacity in the world and the second largest in the U.S. based on a population of 19 million people (Blackburn et al., 2019). With urban development blanketing a coastal plain below steep mountains rising to over 3000 m above sea level, the region is vulnerable to flooding disasters from atmospheric river rainfall events that generate fast-moving runoff and floodwater filled with mud and debris that may overwhelm infrastructure (Jones, 2019; Sanders and Grant, 2020).

A 3 m Zgrid was prepared with 756  $1000 \times 1000$  cell tiles that span an area of 6804 km<sup>2</sup> (see Model Domain in Fig. 1). Levee polyline data were obtained from the National Levee Database (US-ACE, 2015) and further edited for coverage and spatial alignment with blockage features (red lines in Fig. 1). Topographic data for the Zgrid were derived from aerial lidar survey data obtained from the United States Geological Survey (USGS) and National Oceanic and Atmospheric Administration (NOAA) for Los Angeles County and Orange County. The topographic data effectively captures the height of most levees, but additional processing of the data was carried out (i.e., hydro-conditioning) for accurate representation of drainage pathways on the land surface (Bales and Wagner, 2009). For example, aerial lidar encounters line-of-sight obstruction of flow pathways from bridges, roads and other structures, leading to gaps in data coverage or non-physical blockage features in the land surface. Here, these errors were corrected by intersecting OpenStreetMap (OSM) road network data (OpenStreetMap Contributors, 2022) with the DEM to identify and correct erroneous changes in road elevations. A second class of

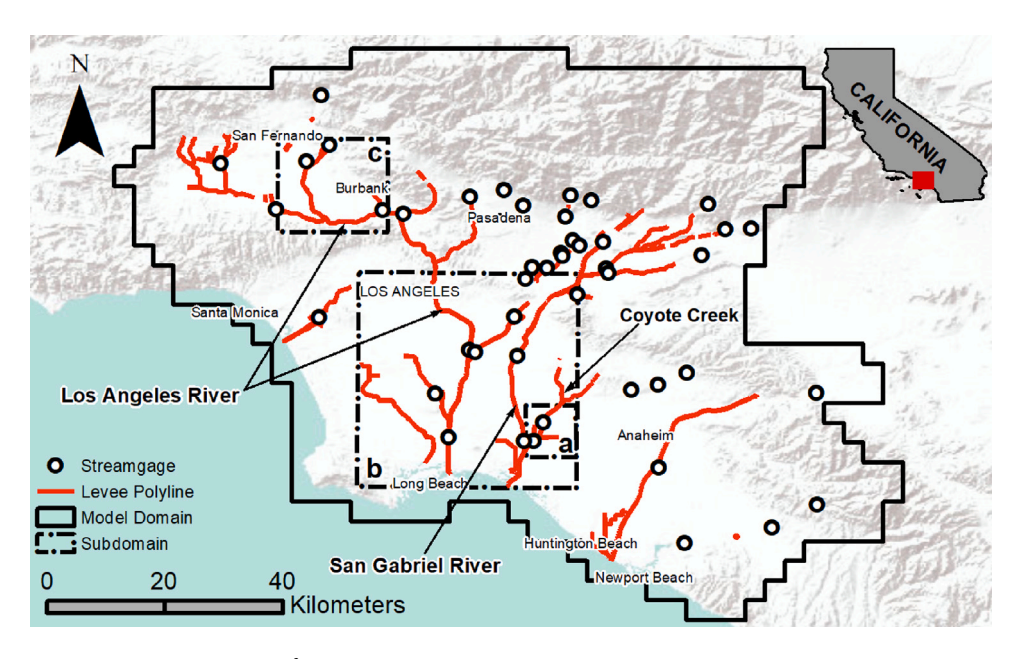


Fig. 1. Fluvial flood hazards are modeled across a  $6804 \text{ km}^2$  domain spanning the Los Angeles Metropolitan Region. A Zgrid consisting of  $756\ 1000 \times 1000$  cell tiles at 3 m resolution is used to resolve topographic heights and the Manning coefficient. Polylines characterize the location of levees (red lines). A 100-year fluvial flooding scenario is created from frequency analysis of 51 streamgage records (circles). Subregions for detailed analysis of model output include: (a) Coyote Creek, (b) Long Beach, and (c) San Fernando.

Table 1
Manning resistance parameters based on land cover/land use.

manning resistance parameters based on land cover, land use.					
Land cover/land use	Manning $n$ (s/m <sup>1/3</sup> )				
Streams	0.01				
Paved surfaces	0.015				
Sandy	0.019				
Undeveloped open space	0.03				
Short grass	0.035				
Developed high intensity	0.02				
Developed open space	0.04				
Long grass	0.05				
Developed medium intensity	0.06				
Agricultural/forested	0.1				
Buildings	0.3				

problems arises with drainage pathways through subsurface pipes, which are not resolved by aerial lidar surveys. Using urban drainage geometry data representing open channels and connecting culverts from Los Angeles County and Orange County Public Works, open channel pathways were "burned" into the DEM to support open channel flow routing. As a result of hydro-conditioning the Zgrid, the Los Angeles Metropolitan Region model developed here resolves both Level 1 infrastructure (major channels and levees) and Level 2 infrastructure (secondary drainage channels and culverts/pipes). However, Level 3 infrastructure (curb inlets and small storm pipes that connect curb inlets to large pipes or channels) are not integrated into the model for this study. A 3 m resolution raster grid of Manning coefficients was also developed for flow resistance based on OSM land use information (see Table 1).

# 2.3. Proposed edge classification

Herein we present a five-step process or workflow (Fig. 2) to improve the representation of levees along Ugrid edges. The process begins with a spatial domain of interest that is spanned by a Ugrid, Zgrid, and levee location data in a polyline format,  $\mathcal{P} = \{(x_1, y_1), (x_2, y_2), \dots, (x_n, y_n)\}$ , and ends with the estimation of edgebased elevation data,  $\hat{z}_k$ ,  $k = 1, \dots, \alpha$ , along edges of the Ugrid. The workflow is illustrated with a channel junction from the Coyote Creek subdomain of the Los Angeles Metropolitan Region (Fig. 1a), as follows:

- 1. The first step (Fig. 2a) involves manual or semi-automated editing of  $\mathcal P$  such that levee polylines delineate both sides of any channel with a levee or flood wall on either side. Levee polylines may be acquired from available repositories (e.g. National Levee Database, openDELvE) and may also be created using geospatial tools
- 2. The second step (Fig. 2b) involves intersecting levee polylines with Ugrid cells to establish a logical matrix M (or mask) at the same size and resolution as the Ugrid, whereby true indicates that the grid cell contains a levee, and false indicates that it does not. This is accomplished by breaking the polylines into a set of points with a linear spacing comparable to  $\Delta_z$ , and flagging all Ugrid cells that contain one or more of these points.
- 3. The third step (Fig. 2c) involves filling holes within the logical matrix, M. These holes correspond to the channel space between levees on opposite sides of a channel. This is accomplished using the imfill command in Matlab (Mathworks, Natick, MA),

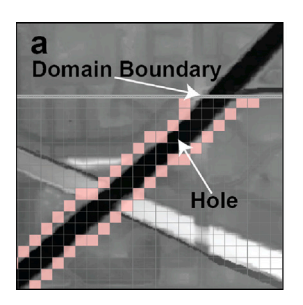
$$M' = \text{imfill}(M, \mathcal{H}) \tag{2}$$

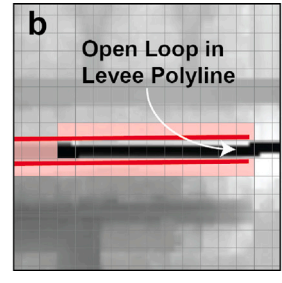
where  $\mathcal{H} = \{(x_1, y_1), (x_2, y_2), \dots, (x_m, y_m)\}$ , represent the coordinates of points within the m holes of the mask  $\mathbf{M}$ . In Fig. 2b, there is only one hole indicated by black coloring, and the hole is filled as shown by the red mask in Fig. 2c. We also note based on experience using the imfill command that the majority of holes are filled automatically, so only a limited number of hole coordinates are typically required. Several iterations of inspecting results and adding additional points are typically required to complete the step.

An important consideration for this stage of the workflow to be successful is whether channel areas are fully encircled by M= true cells. If not, then manual editing of M or the polyline data which generates M (Step 2) will be needed to produce channel areas that are completely surrounded and/or encompassed by M= true cells.

4. The fourth step involves classifying edges of the Ugrid to guide the calculation of  $\hat{z}$  using Zgrid data. Ugrid edges that are representative of levees correspond to edges of the region defined by  $\mathbf{M'}=\mathtt{true}$  and appear in Fig. 2d as blue lines. In the case of vertical grid edges, the edge classification includes three possible options: -1 for when the physical levee is to the

Fig. 2. Grid edge classification proceeds in five steps: (a) delineating the perimeter of flood channels (black) with levee polylines (red), (b) intersecting levee polylines with Ugrid cells to create a mask M, (c) filling interior areas with the Matlab imfill command which creates an updated mask, M', (d) using edges of the M' mask to classify area Ugrid edges as levees (blue lines), and (e) manual editing of Ugrid edges to remove channel blockage.





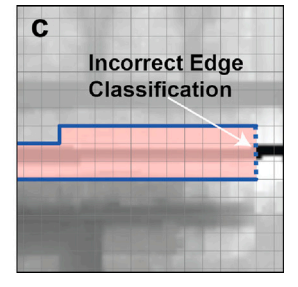


Fig. 3. Application of the grid edge classification method may require manual editing during the workflow to account for (a) channels intersecting the boundary of the model domain and (b) channels with discontinuous levee coverage, which can lead to incorrect edge classifications (c) involving non-physical barriers to channel flow.

left of the Ugrid edge, 0 when there is no levee present, and 1 for when the physical levee is to the right of the Ugrid edge. In the case of horizontal levees, -1 corresponds to a physical levee below the Ugrid edge, and 1 corresponds to a physical levee above the Ugrid edge, and 1 corresponds to a physical levee above the Ugrid edge. The edge classification is saved as two separate arrays for vertical edges and horizontal edges:  $\mathbf{E}^{\mathbf{v}}$ , with a dimension  $(N_x+1,N_y)$  and  $\mathbf{E}^{\mathbf{h}}$ , with dimension  $(N_x,N_y+1)$ , respectively. Mathematically, this classification appears as follows for  $\mathbf{E}^{\mathbf{v}}$ .

$$\mathbf{E}_{I,J}^{\vee} = \begin{cases} -1 & \text{if} & (\mathbf{M}_{I-1,J}' = 1 & \& & \mathbf{M}_{I,J}' = 0) \\ 1 & \text{if} & (\mathbf{M}_{I-1,J}' = 0 & \& & \mathbf{M}_{I,J}' = 1) \\ 0 & \text{otherwise} \end{cases}$$
 (3)

and similarly, elements of Eh are set as follows,

$$\mathbf{E}_{I,J}^{\mathrm{h}} = \begin{cases} -1 & \text{if} & (\mathbf{M}_{I,J-1}' = 1 & \& & \mathbf{M}_{I,J}' = 0) \\ 1 & \text{if} & (\mathbf{M}_{I,J-1}' = 0 & \& & \mathbf{M}_{I,J}' = 1) \\ 0 & \text{otherwise} \end{cases}$$
 (4)

5. In the fifth step, manual re-classification may be required to avoid blockage features in channels. Fig. 2e presents an example where the initial levee polyline data (Fig. 2a) intersected a secondary drainage channel and the automated steps resulted in a non-physical blockage feature.

The mask editing described in Step 3 and edge re-classification described in Step 5 above are representative of the two types of manual editing that may be needed to implement this method: one is related to the creation of holes within the mask M, which requires the use of the imfill command, and the other is related to the removal of edges incorrectly classified as levees. In a practical, large-scale application as shown in Fig. 1, the need for manual editing can result from channels that intersect the model domain boundary (Fig. 3a), channels with discontinuous levee coverage, which leaves openings in levee polylines (Fig. 3b) that need to be closed manually (Step 1 or 2),

and edges incorrectly classified as levees (Fig. 3c) as a consequence of the openings in levee polylines that are closed manually (Fig. 3b).

The grid edge classification matrices E<sup>v</sup> and E<sup>h</sup> guide the processing of Zgrid data to produce a distribution of topographic data for each edge,  $\hat{z}_k$  with  $k=1,\ldots,\alpha$ , for solution updates as follows: For edges classified as non-levee edges, pairs of Zgrid data from opposite sides of the Ugrid edge are averaged to estimate  $\hat{z}$  as reported by Sanders and Schubert (2019). When the edge is classified as -1,  $\hat{z}_k$  is specified based on data from the Ugrid cell on the left-hand side of the edge. In particular, the maximum z value among the  $\alpha^2$  Zgrid data points in the left-hand Ugrid cell is computed and assigned to all  $\alpha$  values of  $\hat{z}_{k}$ . Conversely, when the edge is classified as +1,  $\hat{z}_k$  is specified based on data from the Ugrid cell on the right-hand side of the edge, and the maximum z value from the Zgrid within the right-hand Ugrid cell is assigned to all  $\alpha$  values representing the edge. Fig. 4 illustrates the transfer of high topographic heights representative of a levee (Fig. 4a) to edges of a Ugrid (Fig. 4b) for the estimation of  $\hat{z}_k$  for  $k = 1, ..., \alpha$ . Note that the levee representation (Fig. 4b) is contiguous along Ugrid edges (no gaps) to enforce a barrier to flow in both horizontal and vertical directions when water levels are below the crest of the levee. Upon exceeding the crest elevation, the model simulates overtopping flows in accordance with mass and momentum fluxes resolved by the approximate Riemann solver and solution updates by the flood inundation model (Sanders and Schubert, 2019).

The proposed method to resolve levees results in spatially variable distributions of  $\hat{z}$  for edges that are classified as 0, while it results in constant values of  $\hat{z}$  across each Ugrid edge classified as a levee (-1 or 1). This could bias the method towards overprediction of flood protection in cases where levee heights vary significantly along the Ugrid cell, such as with a sloping channel as shown in Fig. 4. Other sampling strategies could also be considered to create a distribution of edge-based topographic heights,  $\hat{z}_k$  for  $k=1,\ldots,\alpha$ , but for this study, a simple approach was used to promote continuity of flow barriers and avoid non-physical flood spreading through blockage features. Previous work has emphasized the importance of continuity in the gridded representation of blockage features (Hodges, 2015).

With the implementation of this method in PRIMo, the edge classification matrices are written to a file and loaded at the beginning

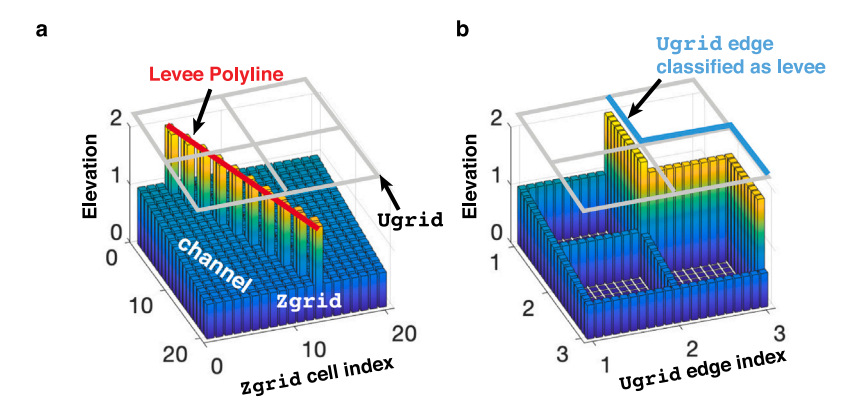


Fig. 4. (a) Topographic data on a Zgrid (bar plot) based on  $\alpha = 10$  including points representative of levees (yellow coloring) are transferred to (b) values along each Ugrid edge,  $\hat{z}_k$ ,  $k = 1, ..., \alpha$ , based on the maximum of the  $\alpha^2$  values within an adjacent grid cell for Ugrid edges classified as levees (-1 or +1, blue line) and a local average of two adjacent Zgrid values for as edges not classified as levees (0, gray lines). Levee polyline data (a, red line) controls edge classification as shown in Fig. 2.

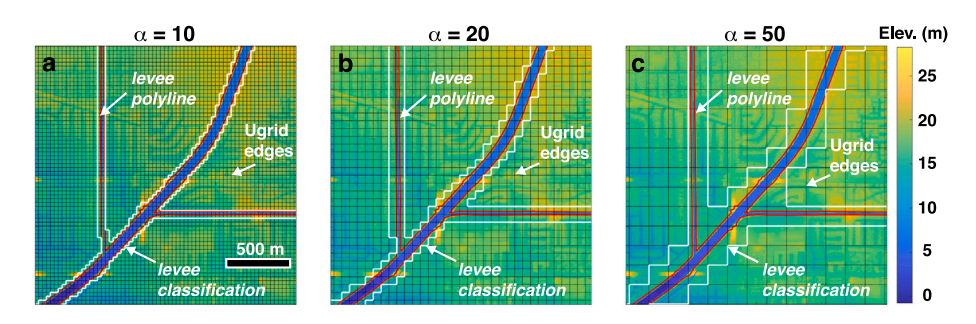


Fig. 5. Coyote Creek edge classification for levees (white lines) on Ugrid (black lines) for upscale factors (α) given by (a) 10, (b) 20 and (c) 50. Original levee polylines (red) and topographic heights (colorbar) resolved by Zgrid are also shown.

of a simulation to guide the computation of edge topography  $(\hat{z}_k, k=1,\dots,\alpha)$  for all edges prior to time-integration. Alternatively, edge topography could be computed off-line and saved in separate sets of files to be loaded at the beginning of the simulation. The former approach was implemented here to minimize the number of input files and the file storage requirements of the model, and because the calculation of edge topography happens very fast in parallel and has negligible impact on overall compute times.

To illustrate the results of this workflow based on data from the Los Angeles region, Ugrid edges classified as levees for the Coyote Creek subdomain (Fig. 1a) are presented in Fig. 5a, b and c (white lines) for  $\alpha=10,\,20$  and 50, respectively. While the representation of levees becomes less precise with increasing upscale factor, the method guarantees two important attributes for flood hazard modeling: first, continuity in flood defenses is preserved irrespective of the upscale factor, which is critical for avoiding artificial leakage through levees; and second, levee heights are based on fine-resolution Zgrid data, irrespective of the upscale factor.

## 2.4. Performance assessment

Fig. 5 shows that as the upscale factor increases, the planform area between levees also increases (note the distance between the white lines and the red lines in Fig. 5), which could affect the accuracy of predictions. Increasing the upscale factor also increases numerical truncation errors (i.e., numerical diffusion) that may impact accuracy. Therefore, simulation accuracy and biases are examined by comparing dual-grid simulations with  $\alpha=5$ , 10, 20, and 50 to fine-grid simulation as has been done in previous studies of flood model performance (e.g., Haile and Rientjes, 2005; Fewtrell et al., 2008). The fine-grid simulation is based on  $\alpha=2$  (6 m) without the edge classification method. Use of  $\alpha=2$  ensures that every topographic data point is used for flux

calculations, and thus all blockage features are resolved for accuracy considerations. A fine-grid model based on  $\alpha=1$  was not possible due to prohibitively expensive compute costs corresponding to simulations fully utilizing 756 compute cores and lasting for many months.

Accuracy and biases in flood extent predictions are evaluated using a contingency table that quantifies the frequency with which the simulation predicts flooded cells (above a threshold of 3 cm) correctly or incorrectly compared to the fine-resolution reference case. The contingency table includes the number of cells correctly predicted as flooded (a), the number of cells where flooded cells are incorrectly predicted to be dry (b), and the number of dry cells incorrectly predicted to be flooded (c). These three measures are used to compute a Critical Success Index (CSI), False Alarm Ratio (FAR), and the Hit Ratio (H) as follows (Schaefer, 1990),

$$CSI = \frac{a}{a+b+c} \qquad , \quad FAR = \frac{c}{a+c} \qquad , \quad H = \frac{a}{a+b}$$
 (5)

where FAR serves as a measure of overprediction, H serves as a measure of underprediction and CSI provides a measure of overall accuracy. We note that a perfect prediction corresponds to CSI = 1, FAR = 0 and H = 1.

Dual-grid model compute times,  $T_{\rm DG}$ , are recorded with all simulations and two different indicators are used as measures of model performance. The first measure is model speed, S, defined as follows,

$$S = \frac{T_{\rm RT}}{T_{\rm DG}} \tag{6}$$

where  $T_{\rm RT}$  represents the real time covered by the simulation, or model duration. The concept of model speed is borrowed from weather forecasting, where model simulations must execute substantially faster than real time to provide timely information. For example, Woods (2006) suggests use of models with S>20 for timely information. Forecasting is not the focus of this study, but given the immense computational

demands of large-scale modeling, compute times are an important consideration, and model speed offers an intuitive dimensionless number to interpret compute costs.

A second measure considered here is the ratio, R, of dual-grid model to single (coarse) grid model compute times,

$$R = \frac{T_{\rm DG}}{T_{\rm SG}} \tag{7}$$

where  $T_{\rm SG}$  represents the compute time of a single-grid model. While no single-grid models are actually implemented in this study, an estimate of single-grid model compute times can be made from a dual-grid model compute time measured under low levels of upscaling.

The compute times of any well-behaved, spatially explicit flood inundation model constrained by the CFL condition can be estimated as follows assuming fixed computing power (Sanders et al., 2010),

$$T = c_0 \frac{1}{A^3} \tag{8}$$

where  $\Delta$  is the grid size and  $c_0$  is a constant that depends on the spatial extent of the model, the real-time duration of the model, and details of the algorithm. Eq. (8) shows that compute times increase by a factor of eight with every halving of the grid size,  $\Delta$ , which illustrates the origin of computational bottlenecks in fine-grid flood inundation modeling. Nevertheless, when compute times are measured at one specific resolution,  $\Delta_0$ , compute times for any other resolution can be estimated by rearranging Eq. (8) as follows,

$$T_{\rm SG}(\Delta) = T_{\rm SG}^0(\Delta_0/\Delta)^3 \tag{9}$$

where  $T_{\rm SG}^0$  represents the compute time for grid size  $\Delta_0$ . For this study, we estimate  $T_{\rm SG}^0$  based on the dual-grid model compute time at very low levels of upscaling ( $\alpha_0=2$ , the finest resolution that was feasible to implement at large scale), and recalling that  $\Delta=\alpha\Delta_z$ , we estimate single-grid model compute times at coarse resolution as follows,

$$T_{SG}(\alpha) = T_{SG}^0(\alpha_0/\alpha)^3 \tag{10}$$

which allows Eq. (7) to be computed as follows,

$$R(\alpha) = \frac{T_{\rm DG}}{T_{\rm SG}^0} (\alpha/\alpha_0)^3 \tag{11}$$

Values of R equal to unity indicate that dual-grid model compute times are equivalent to those of a coarse-grid model, while values greater than unity indicate that the dual-grid model is more computationally demanding than a coarse-grid model at the same coarse-grid resolution.

# 3. Applications

Two test cases are considered, both taken from the Los Angeles Metropolitan Region domain shown in Fig. 1. The first test case utilizes the Coyote Creek subdomain shown in Fig. 1a, while the second test case utilizes the entire domain shown in Fig. 1. Both test cases involve fluvial flood hazard scenarios whereby flooding is forced by point sources of flow added to channels and routed by the flow solver, focusing attention on the accuracy with which coarse-grid flow models characterize levee overtopping and floodplain inundation.

# 3.1. Coyote Creek test case

The Coyote Creek Test Case involves a  $56 \text{ km}^2$  domain with 30 km of levee polylines along three different channels, as shown in Fig. 1a. Fig. 5 provides a magnified view which better illustrates the channel configuration. Topography and resistance are based on a  $2500 \times 2500 \text{ Zgrid}$ , and the grid edge classification method was applied for Ugrids defined by  $\alpha = 5$ , 10, 20, and 50.

This test case is configured to measure the how accurately dualgrid model simulations contain design flows within flood channels, with and without the edge classification method. Point sources of flow are

**Table 2**Flood extent error statistics for Coyote Creek test case compared to a fine-grid model. Perfect accuracy corresponds to CSI=100%, H =100%, and FAR=0%.

α	Unclassified edges			Classified edges		
	CSI (%)	FAR (%)	H (%)	CSI (%)	FAR (%)	H (%)
5	91	7	98	98	0.2	98
10	92	2	94	94	0.1	94
20	74	22	93	92	2	94
50	47	52	97	59	40	97

added to the upstream end of Coyote Creek, Carbon Creek and the unnamed channel west of Coyote Creek at a rate of 800, 225, and 7 m³/s, respectively (see Fig. 5). These flow rates represent 90% of the maximum allowable flow rate in each channel determined empirically, through an iterative process, using model simulations with  $\alpha=2$ . With flow at 90% capacity, simulated overtopping will not occur until there is more than a 10% error in the simulated capacity of the channel. Each simulation was executed from a dry initial condition with steady inflow from point sources and a critical flow outflow boundary condition at the southwest corner of the domain, which yields a subcritical flow regime upstream. A 3-hour model duration was found to be sufficient to reach a steady state and is used in all simulations. Compute times for execution using  $\alpha=2$ , 5, 10, 20, and 50 corresponded to 9.75 h, 30, 5, 1, and < 1 min respectively, on a laptop computer using 4 cores, and there was negligible change to compute times using classified versus unclassified levees

Fig. 6 shows flood extent based on a depth threshold of 3 cm for all model simulations, and flood extent error statistics are reported in Table 2. These results show that the model correctly predicts no levee overtopping for  $\alpha=5$  and 10, and only a minor amount of overtopping (FAR=2%) using  $\alpha=20$ , when using classified edges. In contrast, the model incorrectly predicts moderate levee overtopping (FAR=7%–22%) for  $\alpha=5$  and 20 when using unclassified edges. Use of  $\alpha=50$  results in incorrect prediction of overtopping regardless of the edge classification method, which highlights limits to the amount of upscaling that can be implemented before accuracy levels become unacceptable. To summarize, these results show that the proposed edge classification method reduces or eliminates the incorrect prediction of levee overtopping. For the cases with  $\alpha=5$ , 10 and 20, FAR values are roughly an order of magnitude smaller using classified versus unclassified edges.

# 3.2. Los Angeles Metropolitan Region test case

Application of the edge classification method to the entire Los Angeles Metropolitan domain involved consideration of 987 km of polylines with 92 different channel openings, and levee input files were prepared for Ugrids defined by  $\alpha=5,\,10,\,20,\,$  and 50. Manual editing over several hours was required to address the types of irregularities shown in Figs. 2e and 3.

A 100-year return period fluvial hazard is used to evaluate the grid edge classification at the metropolitan scale. Use of a fluvial scenario focuses attention on the containment of flow in flood channels and potential biases from inaccurate prediction of levee overtopping.

The fluvial flood hazard scenario was developed using data from 51 streamgages across the region maintained by USGS, Los Angeles County Public Works, and Orange County Public Works (see Fig. 1). To estimate 100-year flow rates, frequency analysis was completed using HEC-SSP software developed by the U.S. Army Corps of Engineers (Hydraulic Engineering Center, 2021) which follows USGS Bulletin 17C (England Jr. et al., 2019). Flow was forced with a distributed set of point sources in channels that accumulate to match the 100-year flow rate at each gaging station, in consideration of all upstream point sources. Using 756 compute cores on the Cheyenne cluster at the NCAR-Wyoming Supercomputing Center, flow was simulated for a 48-hour duration to

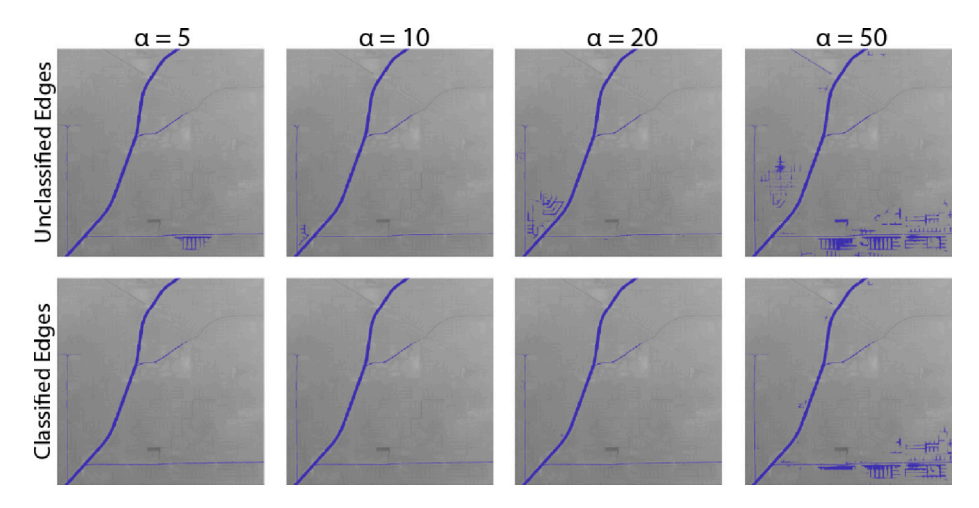


Fig. 6. Simulated flood extent with and without the proposed edge classification method for Coyote Creek test case using  $\alpha = 5, 10, 20, \text{ and } 50.$ 

Table 3 Dual-grid model compute times, model speed S (Eq. (6)), and dual-grid/single-grid compute time ratio R (Eq. (7)) for Los Angeles Metropolitan Region model.

α	Unclassified edges			Classified edges		
	$T_{\rm DG}$ (h)	S	R	$T_{\rm DG}$ (h)	S	R
2	175	0.3	(1)	_	-	-
5	13.8	3.5	1.2	13.1	3.7	1.2
10	1.7	28.2	1.2	1.6	30	1.1
20	0.25	192	1.4	0.16	300	0.9
50	0.07	686	6.3	0.07	686	6.3

reach a steady state, and dual-grid compute time  $T_{\rm DG}$ , model speed S, and the dual-grid/single-grid compute time ratio R are reported in Table 3.

Based on the speed criterion for usefulness reported by Woods (2006) and results in Table 3, model simulations involving  $\alpha=10$ , 20 and 50 provide sufficient speed to provide timely forecast information (i.e., speed is greater than 20). Furthermore, model simulations involving  $\alpha=5$ , 10 and 20 and classified edges have compute costs that closely track the compute costs of an equivalent coarse grid model based on R values close to unity (0.9–1.2). Use of  $\alpha=50$  results in a model speed S that is lower than ideal and a dual-grid/single-grid ratio R that does not match an equivalent single-grid model. We attribute this to the computational demands of data output, which are typically small compared to computing demands, but become a larger fraction of the overall costs as upscaling increases. We also note that our model for single-grid compute times (Eq. (8)) does not account for the cost of data output.

An overview of the flood hazard distribution is presented in Fig. 7, and reveals several parts of the region where channels are unable to contain the 100 year flow rate including communities between Los Angeles and Long Beach (Fig. 7b), communities near Burbank (Fig. 7b), and coastal communities such as Huntington Beach. Fig. 7c-e also show three levels of magnification to illustrate the level of detail that is captured by the model. Fig. 7e shows the finest level of detail characterized by street-level details with flood water moving along the road network.

Of particular interest for this study is whether and to what extent the proposed edge classification method alters the simulated distribution of flooding. To this end, Table 4 provides a summary of flood extent accuracy metrics, using a fine-grid model as a reference case, for the entire model domain as well as Long Beach and San Fernando subdomains shown in Fig. 1. The Long Beach subdomain encompasses a region that was historically occupied by riparian and coastal marshlands of the Los Angeles and San Gabriel Rivers, and is presently defended from flooding by engineered flood channels with levees (Orsi, 2004). Due

Table 4
Flood extent accuracy metrics for Full Domain and Long Beach and San Fernando subdomains shown in Fig. 1.

	α	Unclassified edges			Classified edges			
		CSI (%)	FAR (%)	H (%)	CSI (%)	FAR (%)	H (%)	
Full Domain	5	88	9	96	90	2	92	
	10	81	15	94	87	5	91	
	20	75	21	94	82	12	93	
	50	68	28	92	75	19	90	
Long Beach	5	83	15	97	88	3	90	
	10	76	22	96	88	6	93	
	20	70	28	96	81	16	96	
	50	62	36	96	72	23	93	
San Fernando	5	75	5	78	72	5	75	
	10	61	18	70	61	16	69	
	20	52	30	67	54	26	67	
	50	28	57	45	28	49	38	

to its low topography and position along major rivers, the deepest and most severe flooding of the region is simulated to occur within this subdomain. The San Fernando subdomain is representative of an urbanized alluvial fan where convex topography is capable of producing overtopping flows with diverging flow paths that are highly sensitive to localized changes in topography (NRC, 1996; Garcia et al., 2004; Santangelo et al., 2011). Hence, accuracy metrics are computed in areas of highest importance, based on the depth of flooding, and in areas where high accuracy is expected to be most challenging to achieve.

Table 4 shows that across the Full Domain, the proposed Ugrid edge classification leads to lower FAR and equal or lower H compared to the model with unclassified edges, and the overall accuracy represented by CSI is 2–7 percentage points higher using classified edges. The overall error (computed as 100-CSI) at the scale of the Full Domain can be estimated to be 10, 13 and 18% for  $\alpha=5$ , 10 and 20, respectively. For context, the highest CSI values achieved in validation studies (relative to flood extent measurements) in the study area have been 80%, corresponding to a 20% overall error (Gallegos et al., 2009; Schubert and Sanders, 2012). Hence, the errors of the dual-grid flood model (with grid edge classification) presented here can be viewed, at worst, as being slightly smaller than overall errors considering uncertainty in flow, topography, resistance and storm drain infrastructure.

Table 4 also illuminates different levels of sensitivity to upscaling between the Long Beach and San Fernando subdomains. In the Long

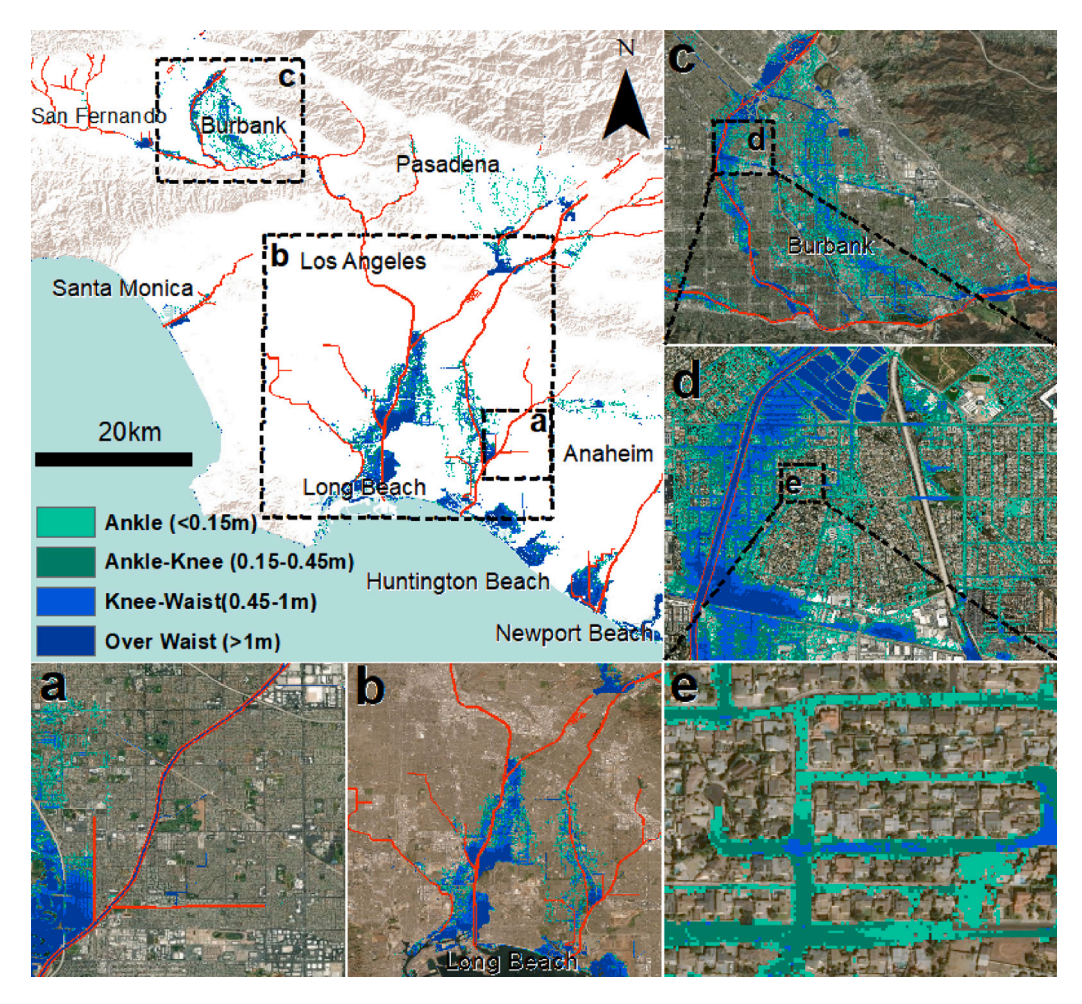


Fig. 7. (a) Simulated flood extent for Los Angeles Metropolitan Region using  $\alpha = 2$ . (b) Long Beach subdomain, (c) San Fernando subdomain, (d) Coyote Creek subdomain, (e) range of scales captured by model.

Beach subdomain where changes in topography are relatively mild and there are numerous channels with levees where overtopping is simulated to occur, the dual-grid model using classified edges yields high accuracy (CSI > 80%) for  $\alpha=5$ , 10 and 20. Conversely, in the San Fernando subdomain characterized as an urbanized alluvial fan, CSI drops to 72 and 61% with  $\alpha=5$  and 10, respectively. Additionally, for the Long Beach subdomain, CSI is increased by 5–12 percentage points, FAR is reduced 12–16 percentage points (less overprediction) and H is reduced 0–7 percentage points (more underprediction) from using classified grid edges. Conversely, in the San Fernando subdomain, FAR is reduced only 0–4 percentage points and H is reduced 0–3 percentage points (excluding the case with  $\alpha=50$ ).

Fig. 8 provides a magnified view of the Long Beach subdomain and shows areas of agreement (green), overprediction (blue), and underprediction (red) compared to the fine-grid model. Overall, the level of agreement appears very good using classified edges, and the amount of underprediction and overprediction appears minimal when using classified edges and  $\alpha=10$ . Additionally, this shows that for all four upscale factors, overprediction is reduced using classified edges compared to unclassified edges (less blue comparing classified to unclassified cases across the same value of  $\alpha$ ). Furthermore, the cause of high overprediction for the case with  $\alpha=50$  and unclassified edges can be attributed to incorrect prediction of channel overtopping (see upper left quadrant of top right panel).

Underprediction may be of particular interest based on the possibility of incorrectly predicting safety from flooding. The amount of underprediction is reflected by the difference between 100% and the hit rate as a percentage. Using classified edges,  $\alpha=5$  yields more

underprediction than  $\alpha=10$ , 20 or 50. Indeed, both the  $\alpha=5$  and  $\alpha=10$  cases result in CSI=88% using classified edges, but the  $\alpha=5$  is better from a perspective of less overprediction and  $\alpha=10$  is better from a less perspective of underprediction.

The patterns of flooding simulated in the San Fernando subdomain are presented in Fig. 9. Flow initiates at the northern edge of the domain where channel capacity is insufficient to contain the 100year flow, and simulated channel overtopping generates divergent flow paths in the downstream (southerly) direction. Note here that a single channel with levees is responsible for the excess flows. Fig. 9 shows that east-west roadways enable dispersal of flooding to the east through neighborhoods. Here, errors in the over- and underprediction of flood extent (blue and red, respectively) strikingly increase between  $\alpha = 20$ and  $\alpha = 50$ . This is attributed to the high sensitivity of alluvial fan flooding to differences in topography resolved by each model (Pelletier et al., 2005). Conversely, differences in flood extent between the classified and unclassified cases are minimal except when using  $\alpha = 50$ . Hence, the results in this sub-domain draw greater attention to the sensitivity of the dual-grid model to increased upscaling versus representation of levees.

# 4. Discussion

As mentioned in the Introduction, urban flood hazards have proven difficult to accurately simulate using large-scale models, and accuracies reported have ranged from CSI=23% (Wing et al., 2017) to CSI=46% (Ward et al., 2017). In these previous studies, CSI is measured relative to flood zones mapped by different models, and thus

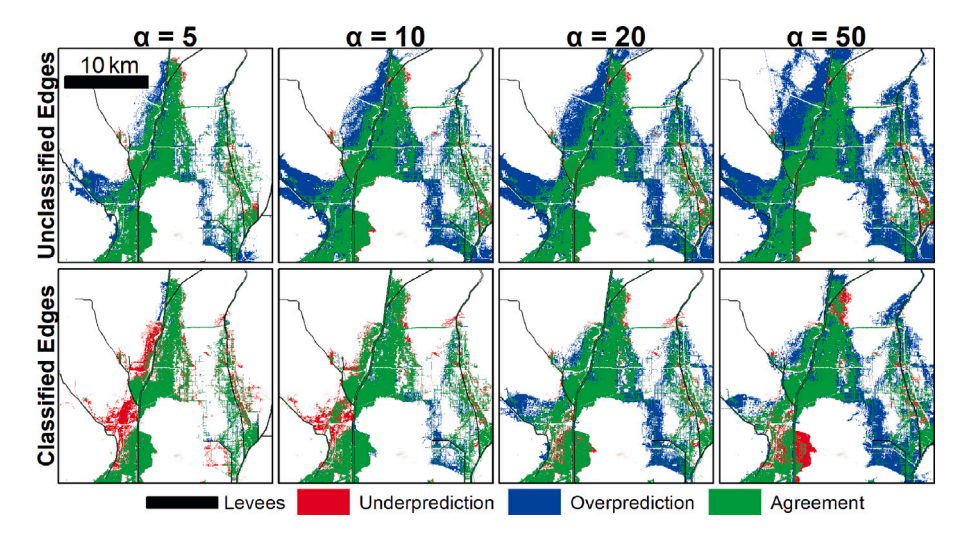


Fig. 8. Flood extent agreement, underprediction, and overprediction of dual-grid model prediction in Long Beach subdomain relative to a fine-grid model.

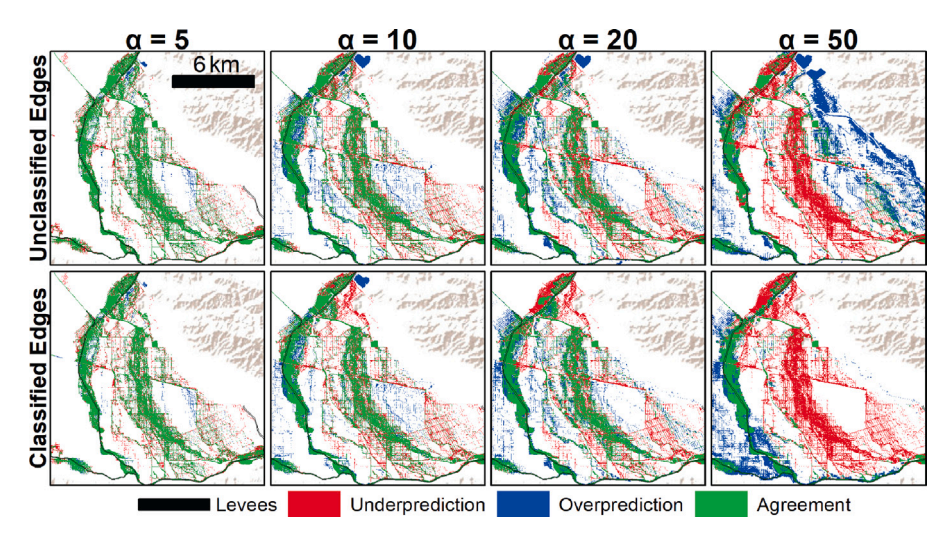


Fig. 9. Flood extent agreement, underprediction, and overprediction of dual-grid model in San Fernando subdomain compared to a fine-grid model.

accounts for numerous factors that contribute to uncertainty such as the magnitude of flood peaks, representation of topography, and other factors. In contrast, CSI values reported here only reflect the effects of upscaling and the proposed Ugrid edge classification. Nevertheless, high CSI values (>80%) demonstrate the potential for large-scale models to reduce errors associated with grid resolution, a finding that is responsive to calls for greater attention to local data for urban flood hazard modeling (e.g., Jonkman, 2013). These results also highlight the challenges of accurate modeling of flood hazards on steep and convex topography associated alluvial fans (see NRC, 1996) based on CSI values of roughly 60% with  $\alpha = 10$  for the San Fernando subdomain (Table 4). These results also demonstrate the value of levee polyline data available from the National Levee Database (USACE, 2015), and the importance of the new global database for levee data, openDELvE (O'Dell et al., 2021). In fact, efforts to utilize levee data in flood hazard modeling studies also present opportunities to scrutinize and further expand existing levee data repositories, and could help to accelerate the availability and coverage of data.

Dual-grid model simulations with forecast-ready speeds (S>20), compute times comparable to those of single-grid models ( $R\approx1$ ) and consistency with respect to fine-grid models (CSI>80%) at the metropolitan scale constitute an important advance with respect to developing flood simulations with fine-grid accuracy at the cost of coarse-grid models. Widespread utilization of dual-grid model structures could

help to improve the accuracy of nationwide flood risk assessments (e.g., Wing et al., 2017; Bates et al., 2021), expand simulation-enhanced flood risk adaptation (e.g., Luke et al., 2018; Sanders et al., 2020) from the community level to the regional level, and enable real-time flood inundation forecasting with a process-based modeling approach (Ivanov et al., 2021). We acknowledge, however, the need for future research to consider the role of Level 3 drainage infrastructure (e.g., curb inlets and small pipe connections to Level 2 drainage infrastructure), and the need for systematic approaches to model calibration and validation. Urban flooding during extreme events is rarely well monitored, and a lack of data for model calibration and validation (e.g., flow and depth distribution through street network) and uncertainties in hydrologic drivers (e.g., precipitation, streamflow, storm surge) hinder the estimation of model parameters and the development of accurate models. Given high uncertainties in hydrologic drivers, it is reasonable to be somewhat pessimistic about achieving major benefits from enhanced land-surface process representation (see Bates, 2012). Additional research is needed on process-based models, strategies for model calibration/validation, and implications for simulation accuracy, timeliness, and uncertainties to deepen understanding and build capacity on this important frontier of hydrologic science and engineering.

#### 5. Summary and conclusion

Herein we present a grid edge classification method to improve the representation of blockage effects and levee overtopping in large-scale, dual-grid flood inundation models that sample topographic data from a fine-resolution Zgrid to account for mass and momentum fluxes between neighboring coarse-resolution Ugrid cells. While previous work envisioned the redistribution of blockage features such as levees along coarse grid edges (e.g., Hodges, 2015; Li and Hodges, 2019, 2020), here we present a new workflow that leverages available polyline data to create a coarse grid edge classification. The workflow sharpens the representation of levees as barriers to flood spreading and constraints on overtopping. Furthermore, we present an application of the workflow that is unprecedented in scale at a fine resolution (3 m), covering the Los Angeles Metropolitan Region, which is home to roughly 19 million people vulnerable to major flooding from a severe atmospheric river event.

Application of the model across the Los Angeles Metropolitan Region shows that flood extent accuracy with  $\alpha = 10$  (30 m effective resolution) is characterized by a critical success index of 87%, a false alarm ratio of 5%, and a hit rate of 91% when compared to a fine-grid model, and compute times are 30 times faster than real time. Similarly, an  $\alpha = 20$  model (60 m effective resolution) achieves a critical success index of 82%, a false alarm ratio of 12%, a hit rate of 93%, and compute times 300 times faster than real time. Furthermore, these dualgrid compute times closely match (within 10%) the compute costs of a single-grid model run at the same coarse-grid resolution. Hence, we find that the proposed grid edge classification method based on levee location data enhances dual-grid model accuracy such that it is comparable to fine-grid model accuracy at compute costs comparable to those of single-grid models. The proposed grid edge classification method is particularly effective at reducing the overprediction of flood extent, which is a drawback of existing dual-grid models (Sanders and Schubert, 2019). This work also validates the importance of the National Levee Database (USACE, 2015), new global levee databases (O'Dell et al., 2021), and accessible, high-resolution topographic databases to enable systematic advances in the modeling of urban flood hazards (Schumann and Bates, 2020).

Differences in dual-grid model accuracy were observed across two subregions of the study area with differing topographical features. In a fluvial corridor near Long Beach historically occupied by riparian and coastal wetlands, the dual-grid model with  $\alpha = 5$  and 10 demonstrated high accuracy marked by a critical success index of 88%. On the other hand, on alluvial fan topography near San Fernando with relatively steep topography, the dual-grid model with  $\alpha = 5$  and 10 demonstrated only moderate accuracy marked by a critical success index of 72 and 61%, respectively. Furthermore, simulated flood extent in the San Fernando subdomain was more sensitive to upscaling than to the proposed grid edge classification. Lower accuracy is attributed to convex topography whereby local-scale variability in the representation of topographic heights can trigger divergent flow paths (NRC, 1996; Pelletier et al., 2005). Furthermore, lower sensitivity to the edge classification method is attributed to flows that far exceed channel capacity such that changes in levee representation do not substantially alter the amount of overtopping flow. These results call attention to the need for more robust dual-grid upscaling methods for steep and convex topography with higher sensitivity to topographic variability.

## CRediT authorship contribution statement

**Daniel T. Kahl:** Methodology, Software, Validation, Formal analysis, Writing – original draft. **Jochen E. Schubert:** Validation, Writing – original draft, Review and editing. **Ariane Jong-Levinger:** Validation, Review and editing. **Brett F. Sanders:** Conceptualization, Methodology, Software, Review and editing, Supervision.

#### **Declaration of competing interest**

The authors declare the following financial interests/personal relationships which may be considered as potential competing interests: Brett F. Sanders reports a relationship with Zeppelin Floods, LLC that includes: equity or stocks. Jochen E. Schubert reports a relationship with Zeppelin Floods, LLC that includes: equity or stocks.

## Data availability

The grid edge classification code is available on github:  $http:/github. \\ com/dtkahl/grid\_edge\_classification$ 

#### Acknowledgments

This research is made possible with support from the National Science Foundation, USA under Grants HDBE-2031535 and ICER-1940171. This work was also supported by the NOAA Effects of Sea Level Rise Program, USA under Grant NA16NOS4780206, and by the Ridge to Reef NSF Research Traineeship, USA, award DGE-1735040. We also acknowledge high performance computing support from the NCAR-Wyoming Supercomputing Center provided by the National Science Foundation and the State of Wyoming, and supported by NCAR's Computational and Information Systems Laboratory.

#### References

- Bales, J., Wagner, C., 2009. Sources of uncertainty in flood inundation maps. J. Flood Risk Manage. 2 (2), 139–147.
- Bates, P.D., 2012. Integrating remote sensing data with flood inundation models: how far have we got? Hydrol. Process. 26 (16), 2515-2521.
- Bates, P.D., Horritt, M.S., Fewtrell, T.J., 2010. A simple inertial formulation of the shallow water equations for efficient two-dimensional flood inundation modelling. J. Hydrol. 387 (1–2), 33–45.
- Bates, P.D., Quinn, N., Sampson, C., Smith, A., Wing, O., Sosa, J., Savage, J., Olcese, G., Neal, J., Schumann, G., et al., 2021. Combined modeling of US fluvial, pluvial, and coastal flood hazard under current and future climates. Water Resour. Res. 57 (2), e2020WR028673.
- Blackburn, S., Pelling, M., Marques, C., 2019. Megacities and the coast: global context and scope for transformation. In: Coasts and Estuaries. Elsevier. pp. 661–669.
- Bradford, S.F., Sanders, B.F., 2005. Performance of high-resolution, nonlevel bed, shallow-water models. J. Eng. Mech. 131 (10), 1073–1081.
- Brunner, G., 2022. HEC-RAS 2D User's Manual. US Army Corps of Engineering Hydraulic Engineering Center, Davis, California, URL: https://www.hec.usace.army.mil/confluence/rasdocs/r2dum/latest.
- Casulli, V., Stelling, G.S., 2011. Semi-implicit subgrid modelling of three-dimensional free-surface flows. Internat. J. Numer. Methods Fluids 67 (4), 441–449.
- Chang, T.-J., Wang, C.-H., Chen, A.S., Djordjević, S., 2018. The effect of inclusion of inlets in dual drainage modelling. J. Hydrol. 559, 541–555.
- Dewals, B., Bruwier, M., Pirotton, M., Erpicum, S., Archambeau, P., 2021. Porosity models for large-scale urban flood modelling: A review. Water 13 (7), 960.
- Dottori, F., Salamon, P., Bianchi, A., Alfieri, L., Hirpa, F.A., Feyen, L., 2016. Development and evaluation of a framework for global flood hazard mapping. Adv. Water Resour. 94, 87–102.
- England Jr., J.F., Cohn, T.A., Faber, B.A., Stedinger, J.R., Thomas, Jr., W.O., Veilleux, A.G., Kiang, J.E., Mason, Jr., R.R., 2019. Guidelines for Determining Flood Flow Frequency—Bulletin 17C. Technical Report, US Geological Survey.
- Fewtrell, T., Bates, P.D., Horritt, M., Hunter, N., 2008. Evaluating the effect of scale in flood inundation modelling in Urban environments. Hydrol. Process. Int. J. 22 (26), 5107–5118.
- Gall, M., Borden, K.A., Emrich, C.T., Cutter, S.L., 2011. The unsustainable trend of natural hazard losses in the United States. Sustainability 3 (11), 2157–2181.
- Gallegos, H.A., Schubert, J.E., Sanders, B.F., 2009. Two-dimensional, high-resolution modeling of urban dam-break flooding: A case study of Baldwin Hills, California. Adv. Water Resour. 32 (8), 1323–1335.
- Gallien, T., Schubert, J., Sanders, B., 2011. Predicting tidal flooding of urbanized embayments: A modeling framework and data requirements. Coast. Eng. 58 (6), 567–577.
- Galloway, G.E., Reilly, A., Ryoo, S., Riley, A., Haslam, M., Brody, S., Highfield, W., Gunn, J., Rainey, J., Parker, S., 2018. The Growing Threat of Urban Flooding: A National Challenge. College Park and Galveston: University of Maryland and Texas A&M University.
- Garcia, R., Rodríguez, J., O'Brien, J., 2004. Hazard zone delineation for urbanized alluvial fans. In: Critical Transitions in Water and Environmental Resources Management. pp. 1–10.

- Guo, K., Guan, M., Yu, D., 2021. Urban surface water flood modelling-a comprehensive review of current models and future challenges. Hydrol. Earth Syst. Sci. 25 (5), 2843–2860.
- Haile, A.T., Rientjes, T., 2005. Effects of LiDAR DEM resolution in flood modelling: a model sensitivity study for the city of tegucigalpa, honduras. In: Isprs Wg Iii/3, Iii/4. Vol. 3. pp. 12–14.
- Hénonin, J., Hongtao, M., Zheng-Yu, Y., Hartnack, J., Havnø, K., Gourbesville, P., Mark, O., 2015. Citywide multi-grid Urban flood modelling: the july 2012 flood in Beijing. Urban Water J. 12 (1), 52–66.
- Henonin, J., Russo, B., Mark, O., Gourbesville, P., 2013. Real-time Urban flood forecasting and modelling-a state of the art. J. Hydroinform. 15 (3), 717-736.
- Hino, M., Nance, E., 2021. Five Ways to Ensure Flood-Risk Research Helps the Most Vulnerable. Nature Publishing Group.
- Hodges, B., 2015. Representing hydrodynamically important blocking features in coastal or riverine lidar topography. Nat. Hazards Earth Syst. Sci. 15 (5), 1011–1023.
- Hydraulic Engineering Center, 2021. HEC-SSP User's Manual version 2.2. Hydrologic Engineering Center. Institute for Water Resources. U.S. Army Corps of Engineers, https://www.hec.usace.army.mil/software/hec-ssp/. (Last Accessed on 2021-12-7).
- Ivanov, V.Y., Xu, D., Dwelle, M.C., Sargsyan, K., Wright, D.B., Katopodes, N., Kim, J., Tran, V.N., Warnock, A., Fatichi, S., et al., 2021. Breaking down the computational barriers to real-time Urban flood forecasting. Geophys. Res. Lett. 48 (20), e2021GL093585.
- Jones, L., 2019. The Big Ones: How Natural Disasters Have Shaped Us (and What We Can Do About Them). Anchor.
- Jongman, B., Winsemius, H.C., Aerts, J.C., De Perez, E.C., Van Aalst, M.K., Kron, W., Ward, P.J., 2015. Declining vulnerability to river floods and the global benefits of adaptation. Proc. Natl. Acad. Sci. 112 (18), E2271–E2280.
- Jonkman, S.N., 2013. Advanced flood risk analysis required. Nature Clim. Change 3 (12), 1004.
- Li, Z., Hodges, B.R., 2019. Modeling subgrid-scale topographic effects on shallow marsh hydrodynamics and salinity transport. Adv. Water Resour. 129, 1–15.
- Li, Z., Hodges, B.R., 2020. On modeling subgrid-scale macro-structures in narrow twisted channels. Adv. Water Resour. 135, 103465.
- Luke, A., Kaplan, B., Neal, J., Lant, J., Sanders, B., Bates, P., Alsdorf, D., 2015. Hydraulic modeling of the 2011 new madrid floodway activation: a case study on floodway activation controls. Nat. Hazards 77 (3), 1863–1887.
- Luke, A., Sanders, B.F., Goodrich, K.A., Feldman, D.L., Boudreau, D., Eguiarte, A., Serrano, K., Reyes, A., Schubert, J.E., AghaKouchak, A., Basolo, V., Matthew, R.A., 2018. Going beyond the flood insurance rate map: insights from flood hazard map co-production. Nat. Hazards Earth Syst. Sci. 18 (4), 1097–1120. http://dx.doi.org/10.5194/nhess-18-1097-2018, URL: https://www.nat-hazards-earth-syst-sci.net/18/1097/2018/.
- Mignot, E., Dewals, B., 2022. Hydraulic modelling of inland urban flooding: recent advances. J. Hydrol. 127763.
- NASEM, 2019. Framing the Challenge of Urban Flooding in the United States. National Academies Press.
- Neal, J., Schumann, G., Bates, P., 2012. A subgrid channel model for simulating river hydraulics and floodplain inundation over large and data sparse areas. Water Resour. Res. 48 (11).
- Noh, S.J., Lee, J.-H., Lee, S., Seo, D.-J., 2019. Retrospective dynamic inundation mapping of hurricane harvey flooding in the houston metropolitan area using high-resolution modeling and high-performance computing. Water 11 (3), 597.
- NRC, N.R.C., 1996. Alluvial Fan Flooding. National Academies Press.
- NRC, N.R.C., 2009. Mapping the Zone: Improving Flood Map Accuracy. The National Academies Press, Washington, DC, http://dx.doi.org/10.17226/12573, URL: https://www.nap.edu/catalog/12573/mapping-the-zone-improving-flood-map-accuracy.
- O'Dell, J., Nienhuis, J.H., Cox, J.R., Edmonds, D.A., Scussolini, P., 2021. A global open-source database of flood-protection levees on river deltas (openDELvE). Nat. Hazards Earth Syst. Sci. Discuss. 1–16.
- OpenStreetMap Contributors, 2022. OpenStreetMap. https://www.openstreetmap.org/. (Last Accessed on 2022-07-21).
- Orsi, J., 2004. Hazardous Metropolis. University of California Press.
- Özer, I.E., van Damme, M., Jonkman, S.N., 2020. Towards an international levee performance database (ILPD) and its use for macro-scale analysis of levee breaches and failures. Water 12 (1), 119.
- Pappenberger, F., Dutra, E., Wetterhall, F., Cloke, H.L., 2012. Deriving global flood hazard maps of fluvial floods through a physical model cascade. Hydrol. Earth Syst. Sci. 16 (11), 4143–4156.
- Pelletier, J.D., Mayer, L., Pearthree, P.A., House, P.K., Demsey, K.A., Klawon, J.E., Vincent, K.R., 2005. An integrated approach to flood hazard assessment on alluvial fans using numerical modeling, field mapping, and remote sensing. Geol. Soc. Am. Bull. 117 (9–10), 1167–1180.
- Russo, B., Sunyer, D., Velasco, M., Djordjević, S., 2015. Analysis of extreme flooding events through a calibrated 1D/2D coupled model: the case of Barcelona (Spain). J. Hydroinform. 17 (3), 473–491.
- Sampson, C.C., Smith, A.M., Bates, P.D., Neal, J.C., Alfieri, L., Freer, J.E., 2015. A high-resolution global flood hazard model. Water Resour. Res. 51 (9), 7358–7381.
- Sanders, B.F., Bradford, S.F., 2006. Impact of limiters on accuracy of high-resolution flow and transport models. J. Eng. Mech. 132 (1), 87–98.
- Sanders, B.F., Grant, S.B., 2020. Re-envisioning stormwater infrastructure for ultrahazardous flooding. Wiley Interdiscip. Rev. Water 7 (2), e1414.

- Sanders, B.F., Schubert, J.E., 2019. PRIMo: Parallel raster inundation model. Adv. Water Resour. 126, 79–95.
- Sanders, B.F., Schubert, J.E., Detwiler, R.L., 2010. ParBreZo: A parallel, unstructured grid, Godunov-type, shallow-water code for high-resolution flood inundation modeling at the regional scale. Adv. Water Resour. 33 (12), 1456–1467.
- Sanders, B.F., Schubert, J.E., Gallegos, H.A., 2008. Integral formulation of shallow-water equations with anisotropic porosity for urban flood modeling. J. Hydrol. 362 (1–2), 19–38.
- Sanders, B.F., Schubert, J.E., Goodrich, K.A., Houston, D., Feldman, D.L., Basolo, V., Luke, A., Boudreau, D., Karlin, B., Cheung, W., et al., 2020. Collaborative modeling with fine-resolution data enhances flood awareness, minimizes differences in flood perception, and produces actionable flood maps. Earth's Future 8 (1), e2019EF001391.
- Santangelo, N., Santo, A., Di Crescenzo, G., Foscari, G., Liuzza, V., Sciarrotta, S., Scorpio, V., 2011. Flood susceptibility assessment in a highly urbanized alluvial fan: the case study of sala consilina (southern Italy). Nat. Hazards Earth Syst. Sci. 11 (10). 2765–2780.
- Schaefer, J.T., 1990. The critical success index as an indicator of warning skill. Weather Forecast. 5 (4), 570–575.
- Schubert, J.E., Sanders, B.F., 2012. Building treatments for urban flood inundation models and implications for predictive skill and modeling efficiency. Adv. Water Resour. 41, 49–64.
- Schumann, G.J.-P., Bates, P., 2020. The Need for a High-Accuracy, Open-Access Global Digital Elevation Model. Frontiers Media SA.
- Schumann, G.J.-P., Stampoulis, D., Smith, A.M., Sampson, C.C., Andreadis, K.M., Neal, J.C., Bates, P.D., 2016. Rethinking flood hazard at the global scale. Geophys. Res. Lett. 43 (19), 10–249.
- Shamkhalchian, A., De Almeida, G.A., 2021. Upscaling the shallow water equations for fast flood modelling. J. Hydraul. Res. 59 (5), 739–756.
- Shustikova, I., Neal, J.C., Domeneghetti, A., Bates, P.D., Vorogushyn, S., Castellarin, A., 2020. Levee breaching: A new extension to the LISFLOOD-FP model. Water 12 (4), 942.
- Stelling, G.S., 2012. Quadtree flood simulations with sub-grid digital elevation models. Proc. Inst. Civ. Eng. 165 (10), 567.
- Task Committee on Flood Safety Policies and Practices, 2014. Flood Risk Management: Call for a National Strategy. American Society of Civil Engineers.
- Teng, J., Jakeman, A.J., Vaze, J., Croke, B.F., Dutta, D., Kim, S., 2017. Flood inundation modelling: A review of methods, recent advances and uncertainty analysis. Environ. Model. Softw. 90, 201–216.
- Tourment, R., Beullac, B., Peeters, P., Pohl, R., Bottema, M., Van, M., Rushworth, A., 2018. European and US Levees and Flood Defences Characteristics, Risks and Governance (Ph.D. thesis). irstea.
- USACE, U.A.C.o.E., 2015. National levee database.
- Valiani, A., Begnudelli, L., 2006. Divergence form for bed slope source term in shallow water equations. J. Hydraul. Eng. 132 (7), 652–665.
- Volp, N., Van Prooijen, B., Stelling, G., 2013. A finite volume approach for shallow water flow accounting for high-resolution bathymetry and roughness data. Water Resour. Res. 49 (7), 4126–4135.
- Ward, P.J., Jongman, B., Aerts, J.C., Bates, P.D., Botzen, W.J., Loaiza, A.D., Hallegatte, S., Kind, J.M., Kwadijk, J., Scussolini, P., et al., 2017. A global framework for future costs and benefits of river-flood protection in Urban areas. Nature Clim. Change 7 (9), 642–646.
- Ward, P.J., Jongman, B., Salamon, P., Simpson, A., Bates, P., De Groeve, T., Muis, S., De Perez, E.C., Rudari, R., Trigg, M.A., et al., 2015. Usefulness and limitations of global flood risk models. Nature Clim. Change 5 (8), 712–715.
- Wing, O.E., Bates, P.D., Neal, J.C., Sampson, C.C., Smith, A.M., Quinn, N., Shustikova, I., Domeneghetti, A., Gilles, D.W., Goska, R., et al., 2019a. A new automated method for improved flood defense representation in large-scale hydraulic models. Water Resour. Res. 55 (12), 11007–11034.
- Wing, O.E., Bates, P.D., Sampson, C.C., Smith, A.M., Johnson, K.A., Erickson, T.A., 2017. Validation of a 30 m resolution flood hazard model of the conterminous United States. Water Resour. Res. 53 (9), 7968–7986.
- Wing, O.E., Lehman, W., Bates, P.D., Sampson, C.C., Quinn, N., Smith, A.M., Neal, J.C., Porter, J.R., Kousky, C., 2022. Inequitable patterns of US flood risk in the anthropocene. Nature Clim. Change 12 (2), 156–162.
- Wing, O.E., Sampson, C.C., Bates, P.D., Quinn, N., Smith, A.M., Neal, J.C., 2019b.
  A flood inundation forecast of hurricane harvey using a continental-scale 2D hydrodynamic model. J. Hydrol. X 4, 100039.
- Winsemius, H.C., Aerts, J.C., Van Beek, L.P., Bierkens, M.F., Bouwman, A., Jongman, B., Kwadijk, J.C., Ligtvoet, W., Lucas, P.L., Van Vuuren, D.P., et al., 2016. Global drivers of future river flood risk. Nature Clim. Change 6 (4), 381–385.
- Winsemius, H., Van Beek, L., Jongman, B., Ward, P., Bouwman, A., 2013. A framework for global river flood risk assessments. Hydrol. Earth Syst. Sci. 17 (5), 1871–1892.
- WMO, W.M.O., 2021. The Atlas of Mortality and Economic Losses from Weather, Climate and Water Extremes (1970–2019). Technical Report, World Meteorological Organization, Geneva, Switzerland, WMO-No. 1267.
- Woods, A., 2006. Medium-Range Weather Prediction: The European Approach. Springer Science & Business Media.